Optical ionization effects in kHz laser wakefield acceleration with few-cycle pulses

J. Monzac, S. Smartsev, J. Huijts, L. Rovige, I A Andriyash, A. Vernier, V. Tomkus, V. Girdauskas, G. Raciukaitis, M. Mackevičiūtė, et al.

Optical ionization effects in kHz laser wakefield acceleration with few-cycle pulses

J. Monzac,[1,*] S. Smartsev,[1] J. Huijts,[1] L. Rovige,[1] I. A. Andriyash,[1] A. Vernier,[1] V. Tomkus,[2] V. Girdauskas,[2,3] G. Raciukaitis,[2] M. Mackevičiūtė,[2] V. Stankevic,[2] A. Cavagna,[1] J. Kaur,[1] A. Kalouguine,[1] R. Lopez-Martens,[1] and J. Faure[1]

[1]*LOA, CNRS, École Polytechnique, ENSTA Paris, Institut Polytechnique de Paris, Palaiseau, France*

[2]*Center for Physical Sciences and Technology, Savanoriu Avenue 231, LT-02300 Vilnius, Lithuania*

[3]*Vytautas Magnus University, K. Donelaicio Street 58, LT-44248 Kaunas, Lithuania*

(Received 25 June 2024; accepted 25 September 2024; published 5 November 2024)

We present significant advances in laser wakefield acceleration (LWFA) operating at a 1 kHz repetition rate, employing a sub-TW, few-femtosecond laser and a continuously flowing hydrogen gas target. We conducted a comprehensive study assessing how the nature of the gas within the target influences accelerator performance. This work confirms and elucidates the superior performance of hydrogen in LWFA driven by few-cycle, low-energy laser pulses. Our system generates quasimonoenergetic electron bunches with energies up to 10 MeV, bunch charges of 2 pC, and angular divergences of 15 mrad. Notably, our scheme relying on differential pumping enables continuous operation at kHz repetition rates, contrasting with previous systems that operated in burst mode to achieve similar beam properties. Particle-in-cell simulations explain hydrogen's superior performances: the ionization effects in nitrogen and helium distort the laser pulse, negatively impacting the accelerator performance. These effects are strongly mitigated in hydrogen plasma, thereby enhancing beam quality. This analysis represents a significant step forward in optimizing and understanding kHz LWFA. It underscores the critical role of hydrogen and the imperative need to develop hydrogen-compatible target systems capable of managing high repetition rates, as exemplified by our differential pumping system. These advances lay the groundwork for further developments in high-repetition-rate laser plasma accelerator technology.

DOI: 10.1103/PhysRevResearch.6.043099

I. INTRODUCTION

Laser wakefield acceleration (LWFA) is an alternative method for accelerating electrons to relativistic velocities [1]. In LWFA, a high-intensity laser pulse generates an accelerating structure, the so-called wakefield, in a plasma. This allows one to surpass the breakdown limit that exists in conventional radio-frequency (rf) cavities: the accelerating fields in the plasma typically reach amplitudes that are four orders of magnitude higher than those in rf cavities. Thus, acceleration occurs over very short distances, paving the way for compact accelerators.

Currently, laser plasma accelerators (LPAs) driven by 100 TW to PW scale laser systems can accelerate electrons to energies ranging from 100 MeV [2] to several GeV over a few centimeters [3–5]. These high-energy LPAs demonstrated electron acceleration up to 8–10 GeV [6,7] using techniques such as laser-guiding or nanoparticle injection. While pushing the energy frontier is important for high-energy physics, current research is also focused on improving the accelerated beam quality and stability of these devices to enable their use in various applications. Indeed, electron beams from LPAs are being considered as drivers for femtosecond x-ray beams, either via betatron radiation [8], Compton scattering [9,10], undulator radiation [11], or free-electron laser radiation [12,13]. Such femtosecond x-ray beams could enable time-resolved (pump-probe) experiments based on, e.g., x-ray diffraction or spectroscopy.

Research on stability improvement has been done, for example, in Ref. [14], where a continuous 24 h experiment was conducted, demonstrating high-quality statistics with 10^5 consecutive electron beams generated at 1 Hz. Additionally, ongoing efforts are focused on developing high-repetition-rate LPAs (100 Hz–kHz), which hold significant potential for improving stability, including the implementation of feedback loops within the accelerator system.

Until recently, kHz laser systems have been limited to a few millijoules per pulse. However, recent progress in optical parametric amplification has enabled the development of higher-energy systems [15]. Ongoing research is pushing the boundaries further, with efforts to achieve Joule-level outputs in kHz systems using Ti:sapphire technology. Additionally, new laser technologies, such as the coherent combination of fiber lasers, thin-disk lasers, and large-aperture Tm:yttrium lithium fluoride (YLF) lasers, are being explored [16]. Still, the few-mJ systems remain compelling due to their compact design and turnkey operation, which make them particularly relevant for various societal applications.

In order to reach relativistic intensities for driving LWFA, the mJ laser pulses require sharp focusing and strong temporal compression, down to nearly a single optical cycle, i.e., a few femtoseconds [17–20]. LPAs driven by few-cycle pulses can

*Contact author: josephine.monzac@ensta-paris.fr

produce electron bunches in the MeV range with pC charge and potentially femtosecond durations.

Femtosecond electron bunches in the 5–10 MeV range are relevant for various applications, including time-resolved electron diffraction [21,22], high-dose rate radiobiology [23–25], and the generation of ultrashort positron beams [26]. For these applications, it is desirable for the accelerator to operate at kHz repetition rates. This poses technical challenges for the gas targets where the plasma is formed and acceleration occurs, as it is difficult to maintain a reasonable vacuum under these conditions.

In [27], Rovige *et al.* demonstrated the continuous and stable operation of a kHz LPA for 5 hours using a free-flowing nitrogen jet. The continuous gas flow in the jet ensures a stable gas density profile even at a kHz repetition rate. Electrons had typical energies of a few MeV and stable beams were achieved thanks to shock injection in an asymmetrically shocked gas jet [28]. Recently, Salehi *et al.* managed to increase the electron energy up to 15 MeV by using a H_2 plasma and kHz, few-cycle laser pulses [29]. However, they were limited to burst-mode operation, as continuous operation led to a deterioration in accelerator performance, likely attributable to the rising background pressure inside the vacuum chamber. Even though the use of lighter gases is more demanding for the pumping system, this work shows that the use of H_2 is beneficial in kHz LPAs driven by few-cycle pulses.

To gain more insight into the influence of the nature of the gas on the properties of the accelerated beams, we have performed a comprehensive study of the impact of the gas used to create the plasma, in the specific frame of few-cycle LWFA. In addition, we demonstrate an operational 1-kHz accelerator working with a continuous flow of H_2, by maintaining a good vacuum in the chamber through a differential pumping scheme. This allowed us to systematically study the influence of three different gases on the accelerated electron beams: nitrogen N_2, helium He, and hydrogen H_2.

The paper is organized as follows: in Sec. II, we recall the various known effects of the gas ionization on the laser pulse. Section III describes the differential pumping system and the experimental apparatus. In Sec. IV, we present the results of the gas comparison study, with additional emphasis on exploring the characteristics of electron beams accelerated with the H_2 plasma. In Sec. V, the injection and acceleration process is investigated through particle-in-cell simulations, and we discuss our interpretations in Sec. VI. before delivering our conclusions in Sec. VII.

II. IONIZATION EFFECTS ON THE LASER PULSE

In terms of energy balance, the ionization process can usually be neglected in LWFA, even for few-mJ pulses. In the particular case of our experiment, the absolute energy loss can be estimated as follows: the energy needed to ionize N_2 up to the fifth level in a cylinder with a 10 μm radius and 200 μm length filled with gas with density $n_N = 2 \times 10^{19}$ cm^{-3} is $E_{\text{ion}} = 0.05$ mJ, which is only 1.8% of the total energy of the laser pulse $E_{\text{laser}} = 2.7$ mJ.

The main detrimental effects of ionization on the laser pulse come from the spatiotemporal distortions that are

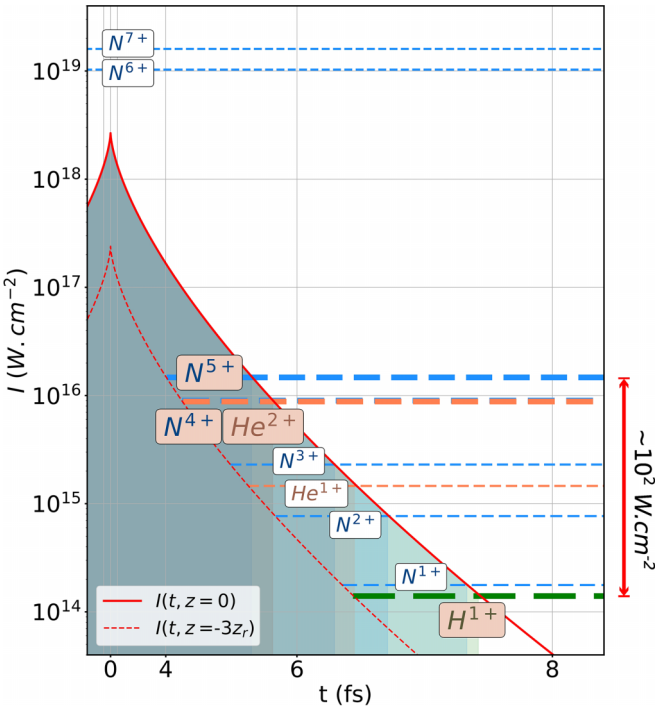

FIG. 1. The laser-intensity profile $I(t)$ at focus (solid red line) and away from focus at $z = -3z_R$ (red dashed line). The horizontal lines correspond to the ionization threshold for the electrons of the different gases [30,31].

imprinted on the laser field. Indeed, the ionization rate varies in space and time. Figure 1 shows the laser-intensity temporal profile $I(t)$ for a Gaussian laser pulse with duration $\tau = 4$ fs at FWHM, and peak intensity $I = 2 \times 10^{18}$ W cm^{-2} at focus, as in our experiment. The dashed lines depict the barrier suppression intensity $I_{bs} = 4 \times 10^9 E_i^4[\text{eV}]/Z^{*2}$ for each ionization level of the three gases [30,31]. Here, E_i is the ionization energy and Z^* is the ionization level of the produced ion. The ionization occurs over very short distances (less than an optical cycle of the laser pulse): there is a front where ionization occurs. H_2 is fully ionized when $I = 1.4 \times 10^{14}$ W cm^{-2}, between 7 and 8 fs before the peak intensity. In addition, the second ionization level of He and the fourth and fifth levels of N_2 are ionized when the laser reaches an intensity $I \simeq 10^{16}$ W cm^{-2}, which is two orders of magnitude higher than for H_2. For a perfectly compressed laser pulse, this implies that the ionization front is at 5–6 fs, significantly closer to the intensity peak so that ionization of these levels will have a larger impact on the laser pulse distortion. This effect is even more pronounced when considering the laser before focus. The red dashed line in Fig. 1 shows the laser-intensity profile at $z = -3z_R$ (which is only ∼180 μm in our experiment), where its intensity is decreased by a factor of 10. Consequently, the ionization front now appears 4 fs before the peak intensity. This suggests even stronger ionization effects that detrimentally impact the spatiotemporal profile of the pulse outside the focal region, as soon as the laser encounters significant gas density.

The first known effect of ionization is spectral/temporal distortion: an ultrafast variation of the refractive index η

results in variations of the instantaneous frequency of the laser pulse [32,33],

$$\Delta\omega = -\frac{\omega_0}{c}\int_0^L \frac{\partial\eta(\mathbf{r},t,z)}{\partial t}dz, \tag{1}$$

where ω_0 is the central frequency, $\mathbf{r}$ is the transverse coordinate, and z is the propagation axis. The refractive index of the plasma is written $\eta = (1-\frac{\omega_p^2}{\omega_0^2})^{1/2}$, where the plasma frequency is $\omega_p^2 = e^2 n_e/m_e\epsilon_0$ with n_e the electronic density of the plasma, and e and m_e the electron charge and mass, respectively. This ionization-induced nonlinear phenomenon results in a frequency blueshift of the laser pulse [34,35].

Second, in the transverse plane, the incoming laser pulse intensity decreases along the radial axis. Therefore, close to the propagation axis, the gas is uniformly ionized, while it is less ionized on the edges of the beam. The electronic density is therefore nonuniform across the laser beam cross section, which causes the plasma to act as a defocusing lens [36]. Then, the laser peak intensity at the focus is reduced, which negatively impacts the properties of the accelerated electron beam.

In practice, both blueshifting and ionization-induced defocusing combine to create spatiotemporal distortions of the laser pulse [37]. Ionization occurs in a small region, smaller than an optical cycle, known as the ionization front. The laser pulse is typically eroded around the ionization front where these effects are strongest, causing the ionization front to shift closer to the peak intensity of the pulse. While this can often be ignored for >30 fs pulses with Joule energy, these effects become particularly critical when dealing with few-mJ few-cycle laser pulses: as the ionization front advances closer to the peak intensity within the laser pulse, ionization-induced distortion becomes increasingly important. Consequently, H_2 should greatly minimize these effects because it has a single ionization level that is two orders of magnitude lower compared to the other available gases, and should therefore be the preferred choice for LPA driven by few-mJ, few-cycle laser pulses.

III. EXPERIMENTAL SETUP

A. Differential pumping for using light gases in continuous operation

Even though H_2 appears ideal to mitigate ionization effects, until now, kHz LWFA experiments with continuous operation have only been performed using N_2 plasma [17,18,20,27]. The use of H_2 has been restricted to burst-mode operation [19,29] because of pumping issues. Regarding the vacuum conditions, using N_2 is more convenient because each molecule provides 10 electrons, while atomic He or molecular H_2 only provide two electrons. Therefore, in order to reach the same electron plasma density with He or H_2, the backing pressure in the gas jet needs to be increased by a factor of about 5, which typically corresponds to 130–150 bar instead of 20–30 bar for N_2 [28]. When applying 20 bar of N_2 in the gas jet, the gas flow rate in the experimental chamber is $Q = 12$ mbar l s^{-1}. Using 100 bar of H_2 in the same gas jet, the leak rate becomes $Q = 224$ mbar l s^{-1}. Moreover, heavy gases are easier to pump than light gases: the compression ratio of the turbomolecular pump goes as $K \propto \exp(\sqrt{M})$, with M the molar mass of the gas, and the pumping speed goes as $S \propto -\ln(K)$ [38,39], so the lighter the gas, the slower the pumping speed of the turbomolecular pump. This has been the bottleneck for using continuous flows of He or H_2 in LWFA.

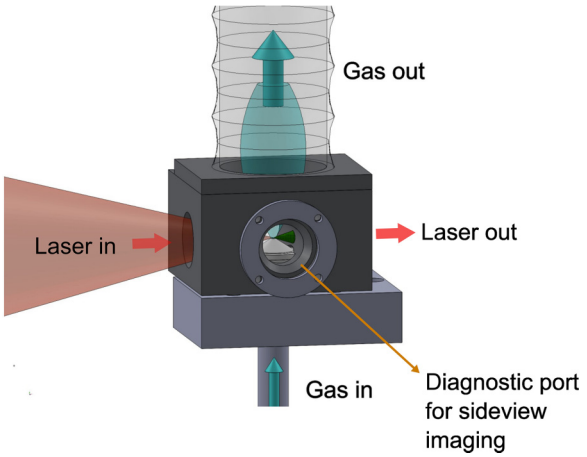

FIG. 2. Three-dimensional (3D) diagram of the differential pumping system. The jet is inside the chamber and two apertures let the laser pass through the chamber, above the gas jet.

To circumvent this issue, we have designed a differential pumping system enabling the use of light gases at high pressure with continuous flow. The differential pumping system is depicted in Fig. 2. It consists of a small vacuum chamber positioned around the gas jet, with two holes to allow the propagation of the laser and the electrons through the chamber. A large dry screw pump with a maximum pumping speed of 650 m^3/h removes the gas directly from this small chamber just above the jet. This system makes it possible to keep the pressure in the main chamber below 10^{-3} mbar, while having a continuous flow of He or H_2 from the nozzle with a backing pressure of up to 150 bar.

B. Laser wakefield accelerator

Laser. The laser wakefield accelerator is driven by the Salle Noire laser facility at the Laboratoire d'Optique Appliquée. It provides 10 mJ, 25 fs FWHM laser pulses at a kilohertz repetition rate, with a central wavelength $\lambda_0 \sim 800$ nm. The laser pulses are spectrally broadened in a hollow-core fiber filled with helium, which expands the spectrum from 650 to 900 nm FWHM through self-phase modulation. Subsequent compression is then achieved using chirped mirrors. The amount of dispersion in the pulse is controlled through a pair of motorized fused silica wedges, permitting one to fine tune pulse compression and measure the temporal intensity profile using the d-scan technique [40]. In the end, the laser delivers vertically polarized 4 ± 0.2 fs pulses at FWHM with 2.7 ± 0.08 mJ on-target energy at 1 kHz repetition rate [41,42]. The pulses are focused by an off-axis parabola down to a 4.5 ± 0.12 μm spot at FWHM, reaching a peak intensity in vacuum $I = 1.8 \times 10^{18}$ W cm^{-2}. The Rayleigh length of the laser beam is $z_r = 62$ μm. The laser is focused at a distance of 150 μm from the exit of a continuously flowing supersonic-shocked gas jet with a 180 μm exit diameter [43,44]. The peak plasma density ranges within $n_e = (5 \pm 0.5) \times 10^{19}$ to $(1.5 \pm 0.15) \times 10^{20}$ cm^{-3}. The hydrodynamic shock within

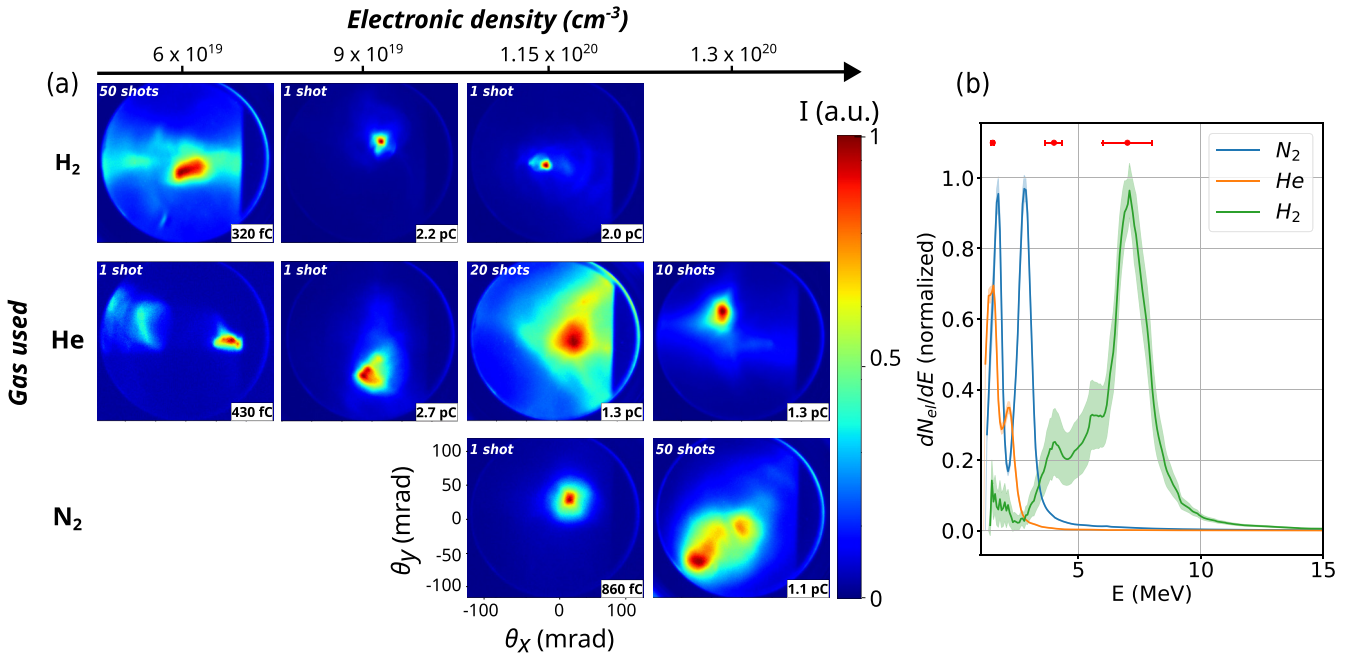

FIG. 3. Experimental results. (a) Variations in electron beam profile as the gas species changes for different values of the electron density. Each image presents an average of 1 to 50 shots, and the color scale is then normalized to its maximum level. (b) Spectra of the electron beam for N_2, He, and H_2 with $n_e = 1.15 \times 10^{20}$ cm^{-3}. The thickness of the lines corresponds to the standard deviation from the mean value estimated over 10 acquisitions for N_2 and He, and 600 acquisitions for H_2. The error bars (in red) correspond to the resolution of the spectrometer at 1.5, 4, and 7 MeV.

the supersonic gas jet creates a downward density gradient, which facilitates and stabilizes the injection of electrons into the wakefield [27,28].

Gas jet. The gas jet that is used is a supersonic-shocked nozzle, as described in [27,28], with a throat diameter 60 μm and an opening diameter 180 μm. Density characterization is performed with N_2 gas, as in [28]: the gas column is illuminated from the side by white light and imaged on a quadriwave lateral shearing interferometer (SID4-HR, Phasics, [45,46]). The electron density for a plasma made of N_2 is then obtained assuming that each molecule is ionized up to the fifth level. In order to find the values for H_2 and He, we assume complete ionization (see Fig. 1). In addition, we used a one-dimensional (1D) isentropic expansion model for compressible gas flows to extrapolate the molecular density in He and H_2. The molecular density in the flow, n_{mol}, can be expressed according to the Mach number M and its initial pressure and temperature, P_0, T_0, in the reservoir [47]:

$$n_{\mathrm{mol}} = \frac{P_0}{k_B T_0}\left(1 + \frac{\gamma - 1}{2}M^2\right)^{-\frac{1}{\gamma-1}}. \qquad (2)$$

Here, the coefficient $\gamma = \frac{C_p}{C_v}$ is the specific-heat ratio of the gas, and k_B is the Boltzmann constant. For our gas jet, where $M \gtrsim 3$, with $P_0 = 40$ bar, we obtain, at the exit of the nozzle, $n_{\mathrm{mol}} = 3.18 \times 10^{19}$ cm^{-3} for N_2, $n_{\mathrm{mol}} = 3.65 \times 10^{19}$ cm^{-3} for He, and $n_{\mathrm{mol}} = 3.19 \times 10^{19}$ cm^{-3} for H_2. Thereafter and throughout this paper, the given electron density corresponds to the density at the plateau of the profile 150 μm above the gas jet. The shock has been characterized in previous work [27,28] and is typically identified by a 20–25% density bump compared to the plateau density.

Electron beam diagnostics. The electron beam charge, spatial profile, and pointing are measured using a calibrated yttrium aluminum garnet (YAG) screen imaged onto a high-dynamic-range CCD camera (14-bit QImaging EXi Blue camera). The beam charge measurement has been cross checked with an integrating charge transformer device [48,49]. Aluminum foils in front of the YAG screen block electrons with energies below 100 keV. The electron energy spectrum is measured onto the same YAG screen by inserting a motorized magnetic spectrometer into the beam. This spectrometer uses two different sets of permanent magnetic dipoles, with magnetic fields of 0.12 and 0.4 T over a 20 mm length respectively, allowing different sensitivities on the electron spectrum.

Data acquisition. Each image presented hereafter was obtained by averaging over 1 to 50 laser shots, depending on the signal level. For each measurement point (i.e., a given value of experimental parameters such as the density, laser pulse duration, etc.), a series of 10 to 500 acquisitions was taken, depending on the required statistics. Statistics over electron beam parameters were then obtained by averaging over an acquisitions series, and the uncertainties represent the root-mean-square (rms) deviation from the mean value.

IV. RESULTS

A. Gas comparison

We examined three different gases: nitrogen, helium, and hydrogen. For each gas, a scan across plasma density n_e was performed. For each measurement pair (gas, n_e), the beam charge and energy were optimized by adjusting the position of the gas jet with respect to the laser focal position, and by

tuning the chirp of the laser pulse. During the optimization process, longitudinal position adjustments were made within a range of $\pm 0.6 z_r$, rendering them negligible.

The angular distributions of the electron beams are presented in Fig. 3(a). The smallest beam divergence is reached in H_2 with an electronic density $n_e = 1.15 \times 10^{20}$ cm^{-3}. It is nearly circular with a divergence of $\Delta\theta = 15.2$ (± 7.0 mrad rms) at FWHM in the laser polarization direction and $\Delta\theta = 13.0$ (± 3.5 mrad rms) FWHM in the perpendicular direction. For the same electronic density, the electron beam from N_2 has a divergence $\Delta\theta = 49$ (± 7.3 mrad rms) FWHM (averaged in the two directions), which is 3.4 times bigger than in H_2. In He, for this particular density, the beam is even larger with a divergence $\Delta\theta = 120$ (± 6 mrad rms) FWHM. However, for higher density, the beam size in He goes down to $\Delta\theta = 42.5$ (± 4.4 mrad rms) FWHM, while the beam size in N_2 increases to $\Delta\theta = 76$ (± 14.9 mrad rms) FWHM. This density could not be reached in H_2 as this would require backing pressures exceeding the limit of our pressure controller (150 bar). The charge of the beam ranges from 1 pC to 3 pC for beams accelerated in He and H_2 at densities higher than 9×10^{19} cm^{-3}, but stays around $\sim$1 pC or less in N_2.

Figure 3(b) represents the spectrum (averaged over 10 acquisitions for N_2 and He, over 600 acquisitions for H_2) of the electrons accelerated in the three gases with electronic density $n_e = 1.15 \times 10^{20}$ cm^{-3}. The thickness of the plot lines corresponds to the rms fluctuations of the data. The red lines correspond to the resolution of the spectrometer. The electron beam accelerated with a H_2 plasma clearly stands out with a peak energy $E_{\text{peak}} = 7$ MeV and the tail of the distribution extending to 10–12 MeV. The width of the peak is limited by the resolution of the spectrometer. For the same density, electron beams from N_2 show a peak at 2.5 MeV, and He shows two peaks at lower energy. We thus observe a threefold energy gain switching from a N_2 or He plasma to a H_2 plasma.

In order to more systematically compare the three gases, we implemented the following merit function: $F(n_e,\ \text{gas}) = \frac{Q \times E_{\text{peak}}}{\Delta\theta}$, with $\Delta\theta$ being the mean of the FWHM of the beam along x and y. This function promotes high-charge beams with a high energy peak and a low beam divergence. Figure 4(a) shows that the beam profile is smaller for electrons accelerated in H_2 plasma. For low densities, the beam in He is smaller than in N_2, but for higher densities, their sizes become similar. Now looking at the merit function, once again H_2 stands out with a merit function that is higher by more than an order of magnitude. Again, He yields better results than N_2 for low densities.

B. Exploring the stability of electron beams in H_2 plasma

Considering the clear advantage of H_2 plasmas, we explored the properties of electron beams generated using a H_2 plasma, focusing on obtaining high-quality and high-stability beams. Figure 5(a) shows the experimental results in a H_2 plasma with $n_e = 6.6 \times 10^{19}$ cm^{-3}. The top part represents 10 acquisitions of the electron beam profile, with each image being averaged over 10 shots. The electron beams have a charge per shot $Q = 970$ fC (± 30 fC rms), which means that the relative rms fluctuations of the charge shot to shot are as low as 3%. The beam pointing has a rms stability of 2 mrad, which means that the electron beam profile has excellent

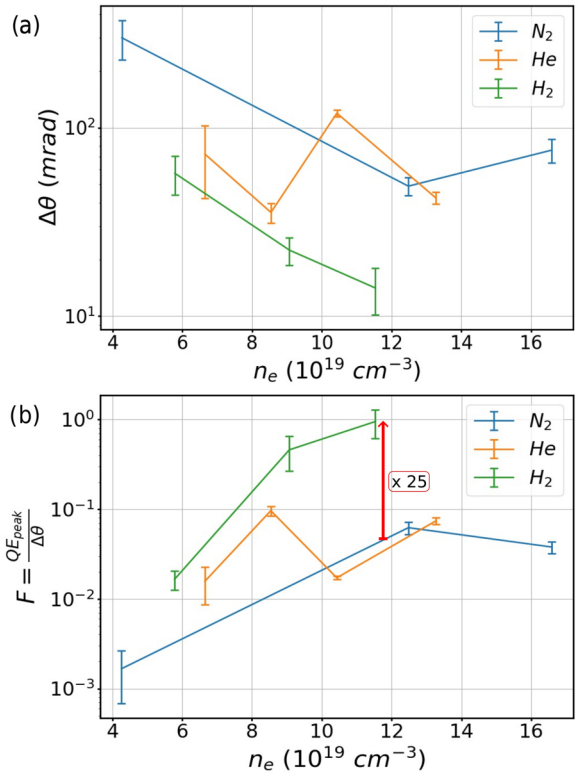

FIG. 4. (a) FWHM beam divergence averaged on both the x and y axes; the smaller the value, the better the beam. Each data point represents an average over at least 10 acquisitions. The vertical error bars indicate the standard deviation from the mean value. (b) Merit function $F(n_e,\ \text{gas}) = Q \times E_{\text{peak}}/\Delta\theta$; the higher the value, the better the beam. The vertical error bars are determined using the uncertainty propagation formula applied to the rms values for each input parameter in F.

stability properties considering its acceleration through LWFA. The lower part of Fig. 5(a) shows the spectrum of the electrons averaged over 10 acquisition (each of 10 laser shots), and the thickness of the line corresponds to the rms fluctuations of the spectrum. The spectrum is quasimonoenergetic with a peak energy of 4.7 MeV (± 0.1 MeV rms), and with an energy spread of 1.45 MeV (± 0.14 MeV rms).

Figure 5(b) shows the stability study of the beam generated using a H_2 plasma with a density $n_e = 8 \times 10^{19}$ cm^{-3}. We recorded 300 randomly sampled acquisitions over 7 minutes, while the accelerator operated at 1 kHz with no active stabilization. For each acquisition, the charge, spectrum, and spatial profile of the electron beam were recorded. The results show an averaged charge $Q = 340$ fC with rms relative fluctuations below 6%, an averaged peak energy $E_{\text{peak}} = 2.7$ MeV with a rms stability as low as 0.7%, and shot-to-shot beam pointing stability of only 2 mrad rms.

V. SIMULATIONS

To understand the difference in performance of the accelerator when using different gases, we performed particle-in-cell (PIC) simulations for the three different gases, while keeping the same laser parameters and final electron plasma density.

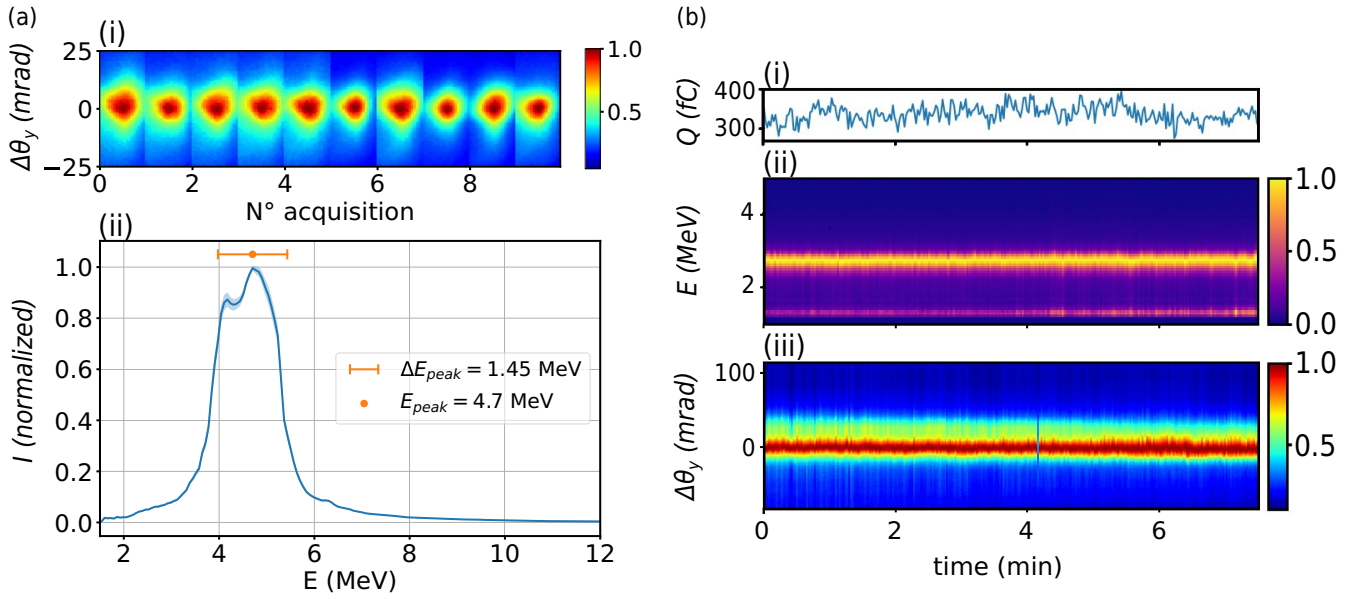

FIG. 5. (a) Experimental results in a H_2 plasma with $n_e = 6.6 \times 10^{19}$ cm^{-3}. (i) Electron beam profile. Each beam profile is obtained with 10 shots. (ii) Spectrum. The spectrum is the result of averaging 100 shots. The thickness of the line corresponds to the rms fluctuations of the spectrum. (b) Characteristics of the electron beam measured continuously over 300 shots (randomly sampled over 7 minutes) at density $n_e = 8 \times 10^{19}$ cm^{-3}. (i) Measured charge, where each point is averaged over 50 shots. (ii) Measured electron spectra, where each spectrum is averaged over 500 shots. (iii) Measured beam divergence, where each profile is a slice of 3 pixels around the measured centroid of the beam averaged over 50 shots.

The modeling is done with the spectral quasi-3D code FBPIC [50], using a cylindrical simulation domain with the grid size $\Delta z = 20.6$ nm, $\Delta r = 2\Delta z$, three azimuthal Fourier modes, and 32 macroparticles of initially neutral gas per cell. The laser duration is 4.2 fs FWHM, with 2.7 mJ energy and a focal spot size of 4.5 μm FWHM, corresponding to the experimental parameters. The gas target is initially neutral and consists of N, He, or H atoms, with number densities adjusted so that the final electron density is the same for all three cases. The density profile is taken from a previous measurement [27] where a similar gas jet was used. The peak electron density is set to reach $n_e = 2 \times 10^{20}$ cm^{-3} after ionization. Special care was taken to ensure that ionization was properly modeled as we expect the ionization process to be a key element to explain the experimental results: (i) all macroparticles are initially neutral and ionization relies on the Ammosov-Delone-Krainov (ADK) tunnel ionization model [30,31], (ii) the laser is initialized at $z = -180$ μm in the simulation so that the propagation of the laser pulse from the entrance of the gas jet is correctly accounted for [see Fig. 6(d) for the representation of the z axis]. Figure 6 shows the result of the PIC simulation and displays the beam profiles [Fig. 6(a)] and the spectra [Fig. 6(b)] of the accelerated electron beams in the three gases. As expected, a higher charge and a better-defined spatial profile are reached in the case of a H_2 plasma compared to the He or N_2 case. Moreover, in H_2, electrons achieve higher energies, with a peak at 8 MeV, while He and N_2 yield a 5 MeV energy peak. The simulations are in good agreement with the trends that are observed in experiments, with better results obtained with a H_2 plasma in terms of charge, energy, and divergence.

These PIC simulations are now used to gain additional insight into the influence of ionization on the acceleration mechanism. The impact of propagation in a ionizing gas can be seen in Fig. 6(c). The electric field of the laser pulse is depicted as a function of the spatial frequency and radial position for the three gases at the time $t = 0.862$ ps, corresponding to propagation within the gas jet at $z = 75$ μm. At this point, the laser pulse has already crossed the density downramp of the jet. Compared to the H_2 plasma, the laser pulse is significantly more distorted and shifted towards higher frequencies in He and N_2 plasmas. This blueshift can be directly attributed to gas ionization [34,35]. Note that ionization-induced defocusing is also visible in the figures for He and N_2 as a transverse broadening of the laser pulse distribution, while it remains minimal for H_2.

Figure 6(d) represents the normalized amplitude of the laser pulse, or normalized vector potential $a_0 = eE/m_e c$, during propagation throughout the gas jet for the three gases under study, along with the theoretical a_0 for propagation in vacuum. In H_2, a_0 reaches 1.8, while in He and N_2, it reaches 1.5 and 1.4, respectively. Notably, He and N_2 exhibit a very similar behavior. Consequently, self-focusing is more effective in H_2 than in He or N_2, as shown by the higher a_0 value. This suggests that the laser pulse experiences greater distortion in He and N_2 compared to H_2, which reduces the self-focusing effect in these gases.

Finally, Fig. 7 illustrates the dynamics of electron injection for the different gases at time $t = 0.862$ ps. The wakefield within the electronic density (shown in green) is driven by the laser pulse, depicted here in orange. Notably, the wakefield exhibits a larger amplitude in the H_2 plasma compared to

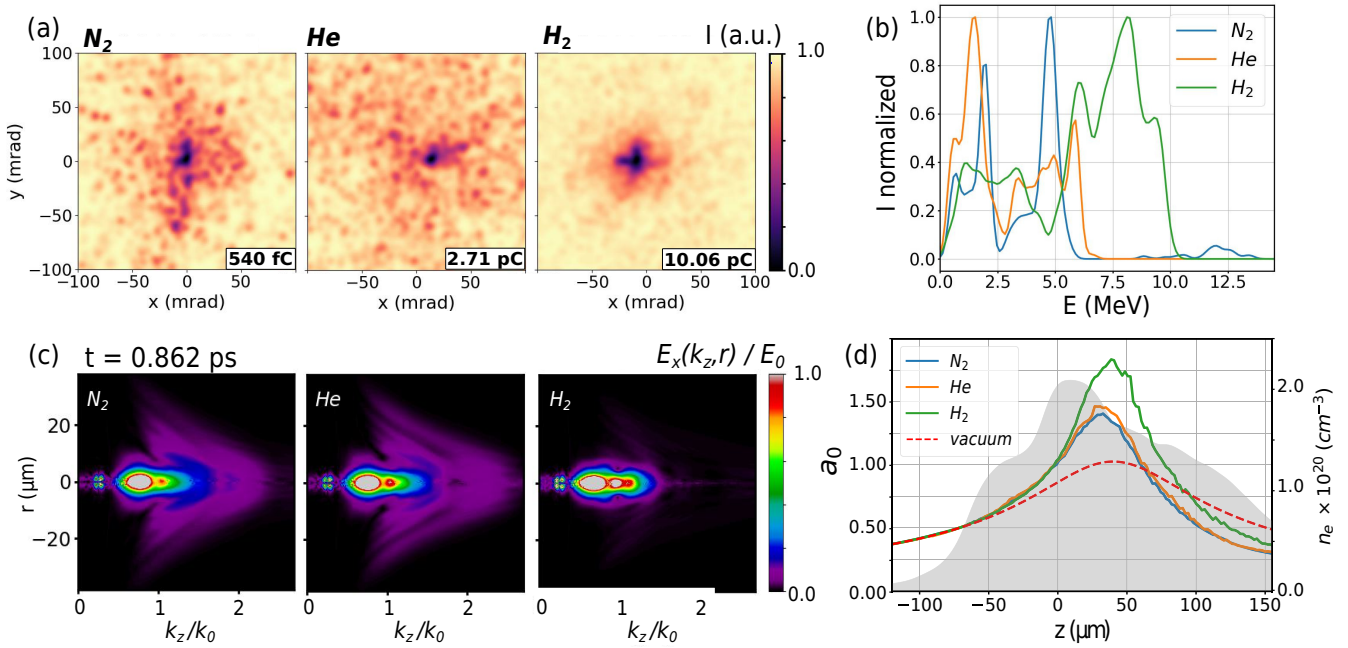

FIG. 6. PIC simulations results. (a) Beam profile and (b) spectra of the simulated beams obtained in N_2, He, and H_2 plasma with $n_e = 1.5 \times 10^{20}$ cm^{-3}, $E_{\text{laser}} = 2.7$ mJ, and $\tau = 4.2$ fs. (c) Spatial spectrum of the laser pulse after propagation at $z = 75$ µm. The images are intentionally saturated to highlight the blueshift and defocusing. (d) Laser normalized amplitude a_0 along the propagation in the plasma z. The gray area represents the density profile of the gas used for the simulations. The density downramp is located at $z \simeq 30$–40 µm.

He or N_2 plasmas. Longitudinal momentum profiles of the injected electrons are plotted in brown as a function of longitudinal position. In the H_2 plasma, electrons are injected around 10 µm behind the laser pulse within the plasma density downramp. In contrast, in the He and N_2 plasmas, electron injection occurs much later, at 30 to 50 µm behind the laser pulse, and accelerated electrons reach lower longitudinal momenta than for the H_2 case.

VI. DISCUSSION

The simulation results confirm that ionization effects induce strong distortions in the laser pulse, manifesting as a blueshift in the spectral domain and ionization-induced defocusing in the spatial domain. These effects degrade the wavefront of the laser pulse during propagation, diminishing its ability to self-focus. Notably, in a H_2 plasma where ionization effects are relatively weak, the laser reaches higher intensity at focus, leading to the generation of a wake with a larger amplitude.

In a stronger wake, electrons are more readily trapped [51,52]. Consequently, in the H_2 plasma, where ionization effects are relatively weak, the stronger wake facilitates rapid trapping of electrons.

In contrast, in the He and N_2 plasmas, the wake amplitude is weaker because the laser intensity itself is weaker. Therefore, electrons are trapped further away from the laser pulse, at a location where the wakefield slows down. We recall the evolution of the wake phase velocity in a nonuniform plasma [53],

$$v_\phi = v_g \frac{1}{1 + (z - v_g t)\frac{1}{k_p}\frac{\partial k_p}{\partial z}} \tag{3}$$

with $k_p(z) = \sqrt{4\pi r_e n_e(z)}$ the local plasma wave number, r_e the classical electron radius, and $(z - v_g t)$ the the laser comoving coordinate. When the distance from the laser pulse $(z_{las} - v_g t)$ increases, the plasma wave slows down, which facilitates the trapping of electrons.

The trapped electrons are injected in the wake with an initial $\gamma \simeq \gamma_\phi = (1 - v_\phi^2/c^2)^{-1/2}$. The closer to the laser the electrons are injected, the higher γ_ϕ. In addition, before entering the decelerating phase, the electrons travel the dephasing length L_{deph} that can be approximated to $L_{\text{deph}} \simeq \gamma_\phi^2 \lambda_p$, where λ_p is the plasma wavelength. Thus, the L_{deph} grows quadratically with the initial momentum of the electrons, $\gamma \sim \gamma_\phi$, which itself depends on the location of injection. In consequence, because injection occurs earlier in H_2, the dephasing length is longer and electrons can reach higher energies.

In addition, the maximum energy gain is not only proportional to L_{deph}, but is also proportional to the amplitude of the electric field of the plasma wake,

$$\Delta E \propto e E_{\text{LWFA}} L_{\text{deph}}. \tag{4}$$

In a H_2 plasma, the wake has a greater amplitude, so the accelerating field is higher and also the dephasing length is longer, as described above. This explains why the electrons accelerated in the H_2 plasma reach higher energies in the experiments. On the contrary, in He and N_2, the laser pulse is distorted because of ionization effects, and thus self-focusing is weaker and the wake has a smaller amplitude. Electron injection occurs in buckets further away from the laser where the wakefield is slow enough to trap plasma electrons. Thus, accelerated electrons experience less intense accelerating fields for a shorter accelerating length, explaining the lower energies. Indeed, PIC simulations (see the electron longitudinal

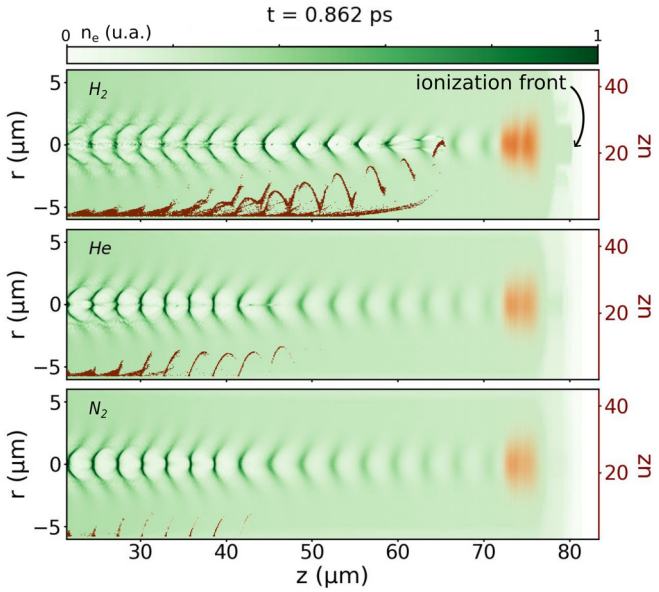

FIG. 7. PIC simulation results at simulation time $t = 0.862$ ps. Images show the laser pulse (orange), plasma wakefield (electronic density in green), and injected electrons longitudinal momentum $u_z = p_z/m_e c$ (brown) in longitudinal phase space. Each line correspondd to the results in one gas, from top to bottom: H_2, He, and N_2.

phase space in Fig. 7) confirm that the electrons injected far from the laser pulse dephase and undergo a decelerating field. In this case, the electrons might cross defocusing regions of the wake, which could also explain why they display a much larger divergence than the beams accelerated in the H_2 plasma.

VII. CONCLUSION

These results represent a clear experimental observation of the influence of the gas species on the electron beam quality and its spectrum in a kHz laser wakefield accelerator. Hydrogen clearly stands out from the other gases with higher energies (a threefold increase of the peak energy in H_2 compared to N_2), higher charge, and smaller divergence (down to 13 mrad). Moreover, electrons accelerated in a H_2 plasma display excellent beam pointing and spectrum stability, with a shot-to-shot beam pointing stability down to 2 mrad rms, and a peak energy stable at 0.7% rms, shot to shot. Electrons accelerated in He demonstrate results closer to those accelerated in nitrogen N_2 than in hydrogen H_2, primarily due to similar ionization levels occurring at $I = 10^{16}$ W cm^2. The implementation of the differential pumping system was a key enabler for this study, as it allowed us to conduct our experiments using light gases such as H_2 to produce high-energy kHz electron beams in a continuous-mode operation. PIC simulation results reproduce all of the experimental observations and confirm that ionization effects significantly distort the laser pulse in He and N_2, which is found to be the cause of the loss of performance of the accelerator for these two gases. Our results demonstrate that despite the challenges posed by its pumping system and safety considerations, H_2 consistently outperforms other gases in generating high-quality electron beams due to its unique and low-ionization level. These findings underscore the critical role of gas selection in laser-plasma acceleration, particularly when using few-cycle, few-mJ laser pulses.

The data that support the findings of this study are available from the contact author upon reasonable request.

ACKNOWLEDGMENTS

This project has received funding from the European Union's Horizon 2020 research and innovation programme under Grant Agreement No. JRA PRISE 871124, and Laserlab-Europe and IFAST under Grant Agreement No. 101004730. This project was also funded by the Agence Nationale de la Recherche under Contract No. ANR-20-CE92-0043-01, and benefited from the support of the Institut Pierre Lamoure via the chair Accélération laser-plasma haute cadence. Financial support from the Région Ile-de-France (Contract No. SESAME-2012-ATTOLITE) and the Extreme Light Infrastructure-Hungary Non-Profit Ltd. (Contract No. NLO3.6LOA) is gratefully acknowledged. We also acknowledge Laserlab-Europe, Grant No. H2020 EC-GA 654148, and the research was funded by the Research Council of Lithuania under Grant Agreement No. S-MIP-21-3. This work has benefited from a grant managed by the Agence Nationale de la Recherche (ANR), as part of the program "Investissements d'Avenir" under the reference (ANR-18-EURE-0014).

[1] T. Tajima and J. M. Dawson, Laser electron accelerator, Phys. Rev. Lett. **43**, 267 (1979).

[2] J. Faure, Y. Glinec, A. Pukhov, S. Kiselev, S. Gordienko, E. Lefebvre, J.-P. Rousseau, F. Burgy, and V. Malka, A laser–plasma accelerator producing monoenergetic electron beams, Nature (London) **431**, 541 (2004).

[3] H. T. Kim, V. B. Pathak, K. Hong Pae, A. Lifschitz, F. Sylla, J. H. Shin, C. Hojbota, S. K. Lee, J. H. Sung, H. W. Lee, E. Guillaume, C. Thaury, K. Nakajima, J. Vieira, L. O. Silva, V. Malka, and C. H. Nam, Stable multi-GeV electron accelerator driven by waveform-controlled PW laser pulses, Sci. Rep. **7**, 10203 (2017).

[4] K. Oubrerie, A. Leblanc, O. Kononenko, R. Lahaye, I. A. Andriyash, J. Gautier, J.-P. Goddet, L. Martelli, A. Tafzi, K. T. Phuoc, S. Smartsev, and C. Thaury, Controlled acceleration of GeV electron beams in an all-optical plasma waveguide, Light Sci. Appl. **11**, 180 (2022).

[5] B. Miao, J. E. Shrock, L. Feder, R. C. Hollinger, J. Morrison, R. Nedbailo, A. Picksley, H. Song, S. Wang, J. J. Rocca, and H. M. Milchberg, Multi-GeV electron bunches from an all-optical laser wakefield accelerator, Phys. Rev. X **12**, 031038 (2022).

[6] A. J. Gonsalves, K. Nakamura, J. Daniels, C. Benedetti, C. Pieronek, T. C. H. de Raadt, S. Steinke, J. H. Bin, S. S. Bulanov,

J. van Tilborg, C. G. R. Geddes, C. B. Schroeder, C. Toth, E. Esarey, K. Swanson, L. Fan-Chiang, G. Bagdasarov, N. Bobrova, V. Gasilov, G. Korn *et al.*, Petawatt laser guiding and electron beam acceleration to 8 GeV in a laser-heated capillary discharge waveguide, Phys. Rev. Lett. **122**, 084801 (2019).

[7] C. Aniculaesei, T. Ha, S. Yoffe, L. Labun, S. Milton, E. McCary, M. M. Spinks, H. J. Quevedo, O. Z. Labun, R. Sain, A. Hannasch, R. Zgadzaj, I. Pagano, J. A. Franco-Altamirano, M. L. Ringuette, E. Gaul, S. V. Luedtke, G. Tiwari, B. Ersfeld, E. Brunetti *et al.*, The acceleration of a high-charge electron bunch to 10 GeV in a 10-cm nanoparticle-assisted wakefield accelerator, Matter Radiat. Extrem. **9**, 014001 (2024).

[8] A. Rousse, K. T. Phuoc, R. Shah, A. Pukhov, E. Lefebvre, V. Malka, S. Kiselev, F. Burgy, J.-P. Rousseau, D. Umstadter, and D. Hulin, Production of a keV x-ray beam from synchrotron radiation in relativistic laser-plasma interaction, Phys. Rev. Lett. **93**, 135005 (2004).

[9] K. Ta Phuoc, S. Corde, C. Thaury, V. Malka, A. Tafzi, J. P. Goddet, R. C. Shah, S. Sebban, and A. Rousse, All-optical Compton gamma-ray source, Nat. Photon. **6**, 308 (2012).

[10] S. Chen, N. D. Powers, I. Ghebregziabher, C. M. Maharjan, C. Liu, G. Golovin, S. Banerjee, J. Zhang, N. Cunningham, A. Moorti, S. Clarke, S. Pozzi, and D. P. Umstadter, MeV-Energy X rays from inverse Compton scattering with laser-wakefield accelerated electrons, Phys. Rev. Lett. **110**, 155003 (2013).

[11] M. Fuchs, R. Weingartner, A. Popp, Z. Major, S. Becker, J. Osterhoff, I. Cortrie, B. Zeitler, R. Horlein, G. D. Tsakiris, U. Schramm, T. P. Rowlands-Rees, S. M. Hooker, D. Habs, F. Krausz, S. Karsch, and F. Grüner, Laser-driven soft-x-ray undulator source, Nat. Phys. **5**, 826 (2009).

[12] W. Wang, K. Feng, L. Ke, C. Yu, Y. Xu, R. Qi, Y. Chen, Z. Qin, Z. Zhang, M. Fang, J. Liu, K. Jiang, H. Wang, C. Wang, X. Yang, F. Wu, Y. Leng, J. Liu, R. Li, and Z. Xu, Free-electron lasing at 27 nanometres based on a laser wakefield accelerator, Nature (London) **595**, 516 (2021).

[13] M. Khojoyan, F. Briquez, M. Labat, A. Loulergue, O. Marcouille, F. Marteau, G. Sharma, and M. E. Couprie, Transport studies of LPA electron beam towards the FEL amplification at COXINEL, Nucl. Instrum. Methods Phys. Res., Sect. A, **829**, 260 (2016).

[14] A. R. Maier, N. M. Delbos, T. Eichner, L. Hubner, S. Jalas, L. Jeppe, S. W. Jolly, M. Kirchen, V. Leroux, P. Messner, M. Schnepp, M. Trunk, P. A. Walker, C. Werle, and P. Winkler, Decoding sources of energy variability in a laser-plasma accelerator, Phys. Rev. X **10**, 031039 (2020).

[15] R. Budriūnas, T. Stanislauskas, J. Adamonis, A. Aleknavičius, G. Veitas, D. Gadonas, S. Balickas, A. Michailovas, and A. Varanavičius, 53 W average power CEP-stabilized OPCPA system delivering 5.5 TW few cycle pulses at 1 kHz repetition rate, Opt. Express **25**, 5797 (2017).

[16] L. Kiani, T. Zhou, S.-W. Bahk, J. Bromage, D. Bruhwiler, E. M. Campbell, Z. Chang, E. Chowdhury, M. Downer, Q. Du, E. Esarey, A. Galvanauskas, T. Galvin, C. Häfner, D. Hoffmann, C. Joshi, M. Kanskar, W. Lu, C. Menoni, M. Messerly *et al.*, High average power ultrafast laser technologies for driving future advanced accelerators, J. Inst. **18**, T08006 (2023).

[17] D. Guenot, D. Gustas, A. Vernier, B. Beaurepaire, F. Bohle, M. Bocoum, M. Lozano, A. Jullien, R. Lopez-Martens, A. Lifschitz, and J. Faure, Relativistic electron beams driven by kHz single-cycle light pulses, Nat. Photon. **11**, 293 (2017).

[18] D. Gustas, D. Guenot, A. Vernier, S. Dutt, F. Bohle, R. Lopez-Martens, A. Lifschitz, and J. Faure, High-charge relativistic electron bunches from a kHz laser-plasma accelerator, Phys. Rev. Accel. Beams **21**, 013401 (2018).

[19] F. Salehi, A. J. Goers, G. A. Hine, L. Feder, D. Kuk, B. Miao, D. Woodbury, K. Y. Kim, and H. M. Milchberg, MeV electron acceleration at 1 kHz with <10 mJ laser pulses, Opt. Lett. **42**, 215 (2017).

[20] J. Faure, D. Gustas, D. Guenot, A. Vernier, F. Bohle, M. Ouille, S. Haessler, R. Lopez-Martens, and A. Lifschitz, A review of recent progress on laser-plasma acceleration at kHz repetition rate, Plasma Phys. Control. Fusion **61**, 014012 (2019).

[21] Z.-H. He, A. G. R. Thomas, B. Beaurepaire, J. A. Nees, B. Hou, V. Malka, K. Krushelnick, and J. Faure, Electron diffraction using ultrafast electron bunches from a laser-wakefield accelerator at kHz repetition rate, Appl. Phys. Lett. **102**, 064104 (2013).

[22] J. Faure, B. van der Geer, B. Beaurepaire, G. Galle, A. Vernier, and A. Lifschitz, Concept of a laser-plasma-based electron source for sub-10-fs electron diffraction, Phys. Rev. Accel. Beams **19**, 021302 (2016).

[23] O. Rigaud, N. O. Fortunel, P. Vaigot, E. Cadio, M. T. Martin, O. Lundh, J. Faure, C. Rechatin, V. Malka, and Y. A. Gauduel, Exploring ultrashort high-energy electron-induced damage in human carcinoma cells, Cell Death Dis. **1**, e73 (2010).

[24] O. Lundh, C. Rechatin, J. Faure, A. Ben-Isma'l, J. Lim, C. De Wagter, W. De Neve, and V. Malka, Comparison of measured with calculated dose distribution from a 120-MeV electron beam from a laser-plasma accelerator, Med. Phys. **39**, 3501 (2012).

[25] M. Cavallone, L. Rovige, J. Huijts, E. Bayart, R. Delorme, A. Vernier, P. G. Jorge, R. Moeckli, E. Deutsch, J. Faure, and A. Flacco, Dosimetric characterisation and application to radiation biology of a kHz laser-driven electron beam, Appl. Phys. B **127**, 57 (2021).

[26] C. Gahn, G. D. Tsakiris, G. Pretzler, K. J. Witte, P. Thirolf, D. Habs, C. Delfin, and C.-G. Wahlstrom, Generation of MeV electrons and positrons with femtosecond pulses from a table-top laser system, Phys. Plasmas **9**, 987 (2002).

[27] L. Rovige, J. Huijts, I. Andriyash, A. Vernier, V. Tomkus, V. Girdauskas, G. Raciukaitis, J. Dudutis, V. Stankevic, P. Gecys, M. Ouille, Z. Cheng, R. Lopez-Martens, and J. Faure, Demonstration of stable long-term operation of a kilohertz laser-plasma accelerator, Phys. Rev. Accel. Beams **23**, 093401 (2020).

[28] L. Rovige, J. Huijts, A. Vernier, I. Andriyash, F. Sylla, V. Tomkus, V. Girdauskas, G. Raciukaitis, J. Dudutis, V. Stankevic, P. Gecys, and J. Faure, Symmetric and asymmetric shocked gas jets for laser-plasma experiments, Rev. Sci. Instrum. **92**, 083302 (2021).

[29] F. Salehi, M. Le, L. Railing, M. Kolesik, and H. M. Milchberg, Laser-accelerated, low-divergence 15-MeV quasimonoenergetic electron bunches at 1 kHz, Phys. Rev. X **11**, 021055 (2021).

[30] M. V. Ammosov, N. B. Delone, and V. P. Krainov, Tunnel ionization of complex atoms and of atomic ions in an alternating electromagnetic field, Sov. J. Exptl. Theor. Phys. **64**, 1191 (1986).

[31] S. Augst, D. Strickland, D. D. Meyerhofer, S. L. Chin, and J. H. Eberly, Tunneling ionization of noble gases in a high-intensity laser field, Phys. Rev. Lett. **63**, 2212 (1989).

[32] E. Yablonovitch, Self-phase modulation and short-pulse generation from laser-breakdown plasmas, Phys. Rev. A **10**, 1888 (1974).

[33] S. C. Wilks, J. M. Dawson, and W. B. Mori, Frequency up-c of electromagnetic radiation with use of an overdense plasma, Phys. Rev. Lett. **61**, 337 (1988).

[34] W. M. Wood, G. Focht, and M. C. Downer, Tight focusing and blue shifting of millijoule femtosecond pulses from a conical axicon amplifier, Opt. Lett. **13**, 984 (1988).

[35] W. M. Wood, C. W. Siders, and M. C. Downer, Measurement of femtosecond ionization dynamics of atmospheric density gases by spectral blueshifting, Phys. Rev. Lett. **67**, 3523 (1991).

[36] S. C. Rae, Ionization-induced defocusing of intense laser pulses in high-pressure gases, Opt. Commun. **97**, 25 (1993).

[37] B. Beaurepaire, D. Guenot, A. Vernier, F. Bohle, M. Perrier, A. Jullien, R. Lopez-Martens, A. Lifschitz, and J. Faure, Limitations in ionization-induced compression of femtosecond laser pulses due to spatiotemporal couplings, Opt. Express **24**, 9693 (2016).

[38] W. Gaede, Die Diffusion der Gase durch Quecksilberdampf bei niederen Drucken und die Diffusionsluftpumpe (The diffusion of gases through mercury vapor at low pressures and the diffusion air pump), Annal. Phys. **351**, 357 (1915).

[39] W. Becker, The turbomolecular pump, its design, operation and theory; calculation of the pumping speed for various gases and their dependence on the forepump, Vacuum **16**, 625 (1966).

[40] M. Miranda, C. L. Arnold, T. Fordell, F. Silva, B. Alonso, R. Weigand, A. L'Huillier, and H. Crespo, Characterization of broadband few-cycle laser pulses with the d-scan technique, Opt. Express **20**, 18732 (2012).

[41] F. Böhle, M. Kretschmar, A. Jullien, M. Kovacs, M. Miranda, R. Romero, H. Crespo, U. Morgner, P. Simon, R. Lopez-Martens, and T. Nagy, Compression of CEP-stable multi-mJ laser pulses down to 4 fs in long hollow fibers, Laser Phys. Lett. **11**, 095401 (2014).

[42] M. Ouille, A. Vernier, F. Bohle, M. Bocoum, A. Jullien, M. Lozano, J.-P. Rousseau, Z. Cheng, D. Gustas, A. Blumenstein, P. Simon, S. Haessler, J. Faure, T. Nagy, and R. Lopez-Martens, Relativistic-intensity near-single-cycle light waveforms at kHz repetition rate, Light Sci. Appl. **9**, 47 (2020).

[43] V. Tomkus, V. Girdauskas, J. Dudutis, P. Gečys, V. Stankevič, and G. Račiukaitis, High-density gas capillary nozzles manufactured by hybrid 3D laser machining technique from fused silica, Opt. Express **26**, 27965 (2018).

[44] A. Marcinkevičius, S. Juodkazis, M. Watanabe, M. Miwa, S. Matsuo, H. Misawa, and J. Nishii, Femtosecond laser-assisted three-dimensional microfabrication in silica, Opt. Lett. **26**, 277 (2001).

[45] J. Primot and L. Sogno, Achromatic three-wave (or more) lateral shearing interferometer, J. Opt. Soc. Am. A **12**, 2679 (1995).

[46] J. Primot and N. Guerineau, Extended Hartmann test based on the pseudoguiding property of a Hartmann mask completed by a phase chessboard, Appl. Opt. **39**, 5715 (2000).

[47] R. D. Zucker and O. Biblarz, *Fundamentals of Gas Dynamics*, 2nd ed. (John Wiley & Sons, Hoboken, NJ, 2002).

[48] K. B. Unser, Design and preliminary tests of a beam intensity monitor for LEP, in *Proceedings of the 1989 IEEE Particle Accelerator Conference, Accelerator Science and Technology, Chicago, IL, USA* (IEEE, 1989), Vol. 1, pp. 71–73.

[49] S.-i. Meigo, H. Nakashima, and H. Takada, Measurement of profile and intensity of proton beam by an integrating current transformer and a segmented parallel-plate ion chamber for the AGS-spallation target experiment (ASTE), Technical Rep. JAERI-Data/Code–2001-014, Japan, 2001.

[50] R. Lehe, M. Kirchen, I. A. Andriyash, B. B. Godfrey, and J.-L. Vay, A spectral, quasi-cylindrical and dispersion-free Particle-In-Cell algorithm, Comput. Phys. Commun. **203**, 66 (2016).

[51] E. Esarey and M. Pilloff, Trapping and acceleration in nonlinear plasma waves, Phys. Plasmas **2**, 1432 (1995).

[52] J. Faure, Plasma injection schemes for laser–plasma accelerators, CERN Yellow Rep. **1**, 143 (2016).

[53] A. V. Brantov, T. Z. Esirkepov, M. Kando, H. Kotaki, V. Y. Bychenkov, and S. V. Bulanov, Controlled electron injection into the wake wave using plasma density inhomogeneity, Phys. Plasmas **15**, 073111 (2008).